

Microscopic description of quadrupole-hexadecapole coupling in radium, thorium, uranium and plutonium isotopes with the Gogny energy density functional

R. Rodríguez-Guzmán^{1,*} and L. M. Robledo^{2,3,†}

¹*Department of Physics, Nazarbayev University, 53 Kabanbay Batyr Ave., Astana 010000, Kazakhstan*

²*Center for Computational Simulation, Universidad Politécnica de Madrid, Campus Montegancedo, 28660 Boadilla del Monte, Madrid, Spain*

³*Departamento de Física Teórica and CIAFF, Universidad Autónoma de Madrid, 28049-Madrid, Spain*

(Dated: February 10, 2025)

The emergence and stability of static hexadecapole deformations as well as the impact in the development of dynamic deformation due to collective motion considering quadrupole-hexadecapole coupling are studied for a selected set of radium, thorium, uranium and plutonium isotopes, using the Gogny Hartree-Fock-Bogoliubov and Generator Coordinate Method frameworks. Sizable hexadecapole deformations are found to play a significant role in the ground and excited states of nuclei in the neighborhood of ^{238}U . For each of the studied isotopic chains, it is shown that a region with small negative hexadecapole deformation, just below the neutron magic number $N = 184$, remains stable once zero-point quadrupole-hexadecapole fluctuations are taken into account. A transition is predicted, with increasing mass number, from a regime in which the quadrupole and hexadecapole degrees of freedom are interwoven to a regime in which they are decoupled, accompanied by an enhanced shape coexistence in the more neutron-rich sectors of the isotopic chains. It is also shown, that quadrupole-hexadecapole configuration mixing brings a nontrivial additional correlation energy gain comparable to the quadrupole correlation energy itself.

PACS numbers: 24.75.+i, 25.85.Ca, 21.60.Jz, 27.90.+b, 21.10.Pc

I. INTRODUCTION.

A significant portion of our present understanding of low-energy nuclear structure hinges on the concept of intrinsic deformation, rooted in the spontaneous symmetry breaking mechanism of (product) mean-field Hartree-Fock-Bogoliubov (HFB) states $|\varphi\rangle$. Nuclear spectra are well known to exhibit fingerprints of several types of shape degrees of freedom associated to intrinsic deformations [1]. Therefore, a better understanding of those degrees of freedom and their interplay, still remains a central issue in nuclear structure nowadays.

Among the multipole moments of the nuclear density, the axial quadrupole moment Q_{20} , associated with the deformation parameter β_2 , is the most relevant and driving one from the energetic point of view. However, other deformations may play a role in specific regions of the nuclear chart. For example, triaxial and/or γ -soft ground states have been predicted in certain regions [2–4], and the impact of (β_2, γ) -deformations on the spectroscopic properties of atomic nuclei, has been studied using a variety of theoretical approaches [5–13]. One should also keep in mind, that the heights of the static inner fission barriers in heavy and super-heavy nuclei are reduced when the γ degree of freedom is included in the calculations [14–17].

In regions with proton and/or neutron numbers around 34, 56, 88 and 134 -where the coupling between intruder $(N + 1, l + 3, j + 3)$ and normal-parity (N, l, j)

states is more pronounced- the spatial reflection symmetry is spontaneously broken [18] and octupole-deformed ground states are favored energetically. Octupole deformation has a strong impact in the outer sectors of the fission paths in heavy and super-heavy nuclei [16, 19, 20] and plays a key role as collective variable in cluster radioactivity [21]. This kind of deformation has received close scrutiny using approaches such as the macroscopic-microscopic (Mac-Mic) model [22, 23], the (mapped) Interacting Boson Model (IBM) [24–30] as well as microscopic approaches, both at the mean-field level and beyond [31–41].

In the case of the Gogny energy density functional (EDF) [42] previous microscopic studies [43–47] have considered the quadrupole-octupole coupling in different regions of the nuclear chart via configuration mixing calculations within the framework of the two-dimensional (2D) Generator Coordinate Method (GCM) [1]. Those studies provided a better understanding of the emergence of static octupole deformation effects within the Gogny-HFB framework and the stability of such effects once dynamical correlations, not explicitly taken into account at the mean-field level, are considered. It has also been found that in most cases, the quadrupole-octupole coupling is rather weak, i.e., to a large extent, the octupole dynamics can be accounted for in one-dimensional (1D) GCM calculations with the octupole deformation as single generating coordinate [43–47].

In comparison with the quadrupole and octupole cases, hexadecapole deformation has received less detailed attention [16, 48–51]. In the case of rare-earth nuclei, this type of deformation can affect the values of the neutrinoless double β decay matrix elements [52]. For a recent

* guzman.rodriguez@nu.edu.kz

† luis.robledo@uam.es

analysis of the impact of hexadecapole deformations on the collective spectra of axially deformed nuclei within the (mapped) IBM approach, the reader is referred to Ref. [53]. In fission calculations, hexadecapole deformations play an important role for near-to-scission configurations [54]. From the experimental point of view, hexadecapole $K^\pi = 4^+$ vibrational bands have been identified [55–57] in previous studies. Both quadrupole and hexadecapole deformations have been inferred from inelastic proton scattering experiments in inverse kinematics on ^{74}Kr and ^{76}Kr [58].

In a recent large-scale HFB survey for even-even nuclei [59], regions of the nuclear chart where static hexadecapole β_4 deformations are favored energetically, have been identified. To this end, calculations were carried out using the parametrization D1S [42] and D1M* [60] of the Gogny-EDF. These Gogny-HFB calculations were followed by an account of the dynamical (β_2, β_4) -coupling in Sm and Gd isotopes within the 2D-GCM framework. A key lesson extracted from those 2D-GCM calculations is that, at variance with the rather weak quadrupole-octupole coupling found in similar calculations [43–47], the quadrupole and hexadecapole degrees of freedom are strongly coupled and, therefore, full-fledged 2D-GCM calculations must be carried out. Furthermore, at least for some of the considered Sm and Gd nuclei, the inclusion of the hexadecapole degree of freedom in the ground state dynamics leads to an additional correlation energy around 500-600 keV, which is similar in size to typical quadrupole correlation energies.

The results mentioned above suggest that it is timely and necessary to examine the nontrivial beyond-mean-field (β_2, β_4) -coupling in regions other than the Sm and Gd isotopic chains, starting from modern EDFs with reasonable predictive power all over the nuclear chart. This is our main goal in this work, devoted to the study of hexadecapole deformation effects and their coupling to the quadrupole degree of freedom in several isotopic chains (Ra, Th, U and Pu) in the actinide region. Our study is also motivated by a recent analysis of hydrodynamic simulations of the elliptic flow in heavy ion collisions involving the creation of a quark-gluon plasma at the BNL Relativistic Heavy Ion Collider (RHIC), which demonstrated the key role of hexadecapole deformation to restore the agreement between the simulations and the available data for collisions of ^{238}U [61].

In this paper, we address the emergence and stability of mean-field hexadecapole deformation effects as well as the impact of the dynamical (β_2, β_4) -coupling in the long isotopic chains $^{232-268}\text{Ra}$ ($Z=88$), $^{232-268}\text{Th}$ ($Z=90$), $^{232-268}\text{U}$ ($Z=92$) and $^{232-268}\text{Pu}$ ($Z=94$). The Z values lie around the region where the largest β_4 values are expected in the actinide region [59]. The reason driving our choice of the mass range $232 \leq A \leq 268$ is, first, to examine both static and dynamic β_4 deformation effects around ^{238}U [61]. Second, the considered mass range extends up to neutron-rich isotopes below the magic neutron number $N = 184$ [16]. It is precisely

in this region where static $\beta_4 < 0$ values are obtained in previous Gogny-HFB calculations [59], in agreement with the predictions of the polar-gap model [62, 63].

To the best of our knowledge, a detailed dynamical analysis of $\beta_4 < 0$ deformation has not yet been presented in the literature. On the other hand, the predicted region with small $\beta_4 < 0$ values requires a dynamical analysis to assess the survival of those weak hexadecapole deformation effects from a beyond-mean-field perspective. Furthermore, such a dynamical analysis is also required since the structural evolution of the mean-field potential energy surfaces (MFPEs) in the considered isotopic chains (see, Sec. III A) reveals that, as we move to more neutron-rich sectors, there is a pronounced competition between low-lying configurations (minima) based on different intrinsic (quadrupole and/or hexadecapole) shapes.

As in previous studies [43–47, 59], we have resorted to a theoretical framework consisting of two steps. First, we have performed HFB calculations with constraints [1] on the axially symmetric quadrupole \hat{Q}_{20} and hexadecapole \hat{Q}_{40} operators. For each of the studied nuclei, the HFB calculations provide the energies $E_{HFB}(\beta_2, \beta_4)$ and the corresponding intrinsic states $|\varphi(\beta_2, \beta_4)\rangle$ labeled by the quadrupole β_2 and hexadecapole β_4 deformation parameters [see, Eq.(1) below]. As a second step, the HFB states $|\varphi(\beta_2, \beta_4)\rangle$ are used as a basis in a 2D-GCM ansatz. Via the solution of the corresponding Griffin-Hill-Wheeler (GHW) equation [1], we study the stability of static hexadecapole deformation effects once zero-point quantum fluctuations in the generating (β_2, β_4) -coordinates are taken into account.

Both at the HFB and 2D-GCM levels, we have resorted to the parametrization D1S of the Gogny-EDF [42]. Such a parametrization has already been shown to provide a reasonable description of several properties, both at the mean-field level and beyond, all over the nuclear chart [64]. The Gogny-D1S parametrization has also been successfully employed, as a reference, in a previous large-scale HFB survey of hexadecapole properties [59]. We have also carried out calculations with the parametrization D1M* [60] and D1M [65]. However, as in previous studies (see, for example, [43–47, 59] and references therein), we have found a very mild dependence of the results on the underlying parametrization of the Gogny-EDF and, therefore, we will not dwell on these details in the present study.

Considering hexadecapole triaxial degrees of freedom would be a natural extension to the present approach as it would give access to study the properties of the $K^\pi = 4^+$ vibrational bands recently identified [55–57]. However, the extra complexity of both going triaxial and dealing at the same time with three collective coordinates makes the calculations extremely expensive.

The paper is organized as follows. The employed theoretical framework is briefly outlined in Sec. II. In particular, the Gogny HFB and 2D-GCM approaches are briefly sketched in Secs. II A and II B. For a more detailed account the reader is referred to Refs. [43, 59, 64]. The

results of the calculations are discussed in Sec. III. First, in Sec. III A attention is paid to the structural evolution of the MFPEs leading to the emergence of (static) positive and/or negative hexadecapole deformation effects in the isotopic chains $^{232-268}\text{Ra}$, $^{232-268}\text{Th}$, $^{232-268}\text{U}$ and $^{232-268}\text{Pu}$. The 2D-GCM results obtained for those nuclei are discussed in Sec. III B. Here, attention is paid to the stability of static β_4 deformation effects and the impact of the beyond-mean-field (β_2, β_4) -coupling via the analysis of quantities such as collective wave functions, dynamical deformation values and correlation energies. Results obtained with 1D-GCM calculations, will also be discussed in this section. In the same section, we examine the interleaving of the quadrupole and hexadecapole degrees of freedom in the excited 2D-GCM states. Finally, Sec. IV is devoted to the concluding remarks.

II. THEORETICAL FRAMEWORK

To study the interplay between the quadrupole and hexadecapole degrees of freedom, both at the (static) HFB and dynamical (2D-GCM) levels, we have resorted in this work to the HFB+2D-GCM scheme [43–47, 59], based on the D1S parametrization of the Gogny force [42]. The key ingredients of the HFB approach are sketched in Sec. II A, while the 2D-GCM scheme is briefly outlined in Sec. II B.

A. The Gogny HFB framework

Our starting theoretical tool is the constrained HFB method [1]. Aside from the usual mean-field constraints on the proton and neutron numbers [1], the HFB equation has been solved with constraints on the axially symmetric quadrupole \hat{Q}_{20} and hexadecapole \hat{Q}_{40} operators. The quadrupole Q_{20} and hexadecapole Q_{40} moments are obtained as average values of the corresponding multipole operators $Q_{\lambda 0} = \langle \varphi | \hat{Q}_{\lambda 0} | \varphi \rangle$ ($\lambda = 2, 4$) in the HFB states $|\varphi\rangle$. We have parameterized the moments $Q_{\lambda 0}$ in terms of the deformation parameters β_λ [66]

$$Q_{\lambda 0} = \frac{3R_0^\lambda A}{\sqrt{4\pi(2\lambda + 1)}} \beta_\lambda \quad (1)$$

with $R_0 = 1.2A^{1/3}$ and A the mass number. Thus, the label $\vec{\beta} = (\beta_2, \beta_4)$ is attached to the HFB energies $E_{HFB}(\vec{\beta})$ and intrinsic states $|\varphi(\vec{\beta})\rangle$. For the solution of the constrained HFB equations, an approximate second order gradient method has been employed [67].

Axial symmetry has been kept as a self-consistent symmetry in the calculation as triaxial shapes are not expected to play a relevant role in the ground state properties. The HFB quasiparticle operators [1] have been expanded in a large axially symmetric harmonic oscillator (HO) basis containing 17 major shells with the oscillator

lengths $b_\perp = b_z = b_0 = 1.01A^{1/6}$. In the HFB calculations all the states $|\varphi(\vec{\beta})\rangle$ are characterized by the same value of the oscillator length b_0 in order to avoid technical difficulties in the application of the extended Wick theorem [68, 69] to the calculation of GCM kernels. To test the convergence with basis size, calculations with 19 major shells have been performed in a handful of cases. The results indicate that apart from a slight increase in the total binding energy, other observables like excitation energies and transition probabilities remain essentially unaltered.

As a result of the mean-field approach, we have obtained a set of intrinsic states and energies in a (β_2, β_4) -mesh with the step sizes $\delta\beta_2 = \delta\beta_4 = 0.01$. Given the possibility to find in the same nucleus coexisting prolate and oblate structures as well as very flat minima in the hexadecapole direction a large deformation domain has been considered in the HFB calculations

$$\mathcal{D}_{\vec{\beta}} = \left\{ \beta_2 \in [-0.8, 1.2]; \beta_4 \in [-0.8, 1.2] \right\} \quad (2)$$

We find that the given domain is enough to account for basic properties in both the ground and excited states of the studied nuclei at the 2D-GCM level.

B. The Gogny 2D-GCM framework

Once the HFB states $|\varphi(\vec{\beta})\rangle$ have been obtained in the deformation domain $\mathcal{D}_{\vec{\beta}}$, they are employed as basis for the 2D-GCM ansatz

$$|\Psi_{2D-GCM}^\sigma\rangle = \int_{\mathcal{D}_{\vec{\beta}}} d\vec{\beta} f^\sigma(\vec{\beta}) |\varphi(\vec{\beta})\rangle \quad (3)$$

where the index σ numbers the ground $\sigma = 1$ and excited $\sigma = 2, 3, \dots$ GCM solutions. We have also introduced the shorthand notation $\vec{\beta} = (\beta_2, \beta_4)$ in the above equation. In the numerical applications the integrals in Eq.(3) have been discretised in the domain $\mathcal{D}_{\vec{\beta}}$ with the step size given above.

A more general GCM ansatz than the one in Eq.(3) would be required to consider the coupling to additional degrees of freedom [70]. Nevertheless, for obvious technical reasons -such as the large number of HO shells used and the large deformation domain employed in the calculations- such a task is out of the scope of this paper, where we will restrict to the use of the $\vec{\beta} = (\beta_2, \beta_4)$ generating coordinates.

The amplitudes $f^\sigma(\vec{\beta})$ in the GCM ansatz of Eq.(3) are determined dynamically via the solution of the GHW equation [1, 43–47, 59]

$$\int_{\mathcal{D}_{\vec{\beta}_2}} d\vec{\beta}_2 \left\{ \mathcal{H}(\vec{\beta}_1, \vec{\beta}_2) - E^\sigma \mathcal{N}(\vec{\beta}_1, \vec{\beta}_2) \right\} f^\sigma(\vec{\beta}_2) = 0 \quad (4)$$

written in terms of non-diagonal norm

$$\mathcal{N}(\vec{\beta}_1, \vec{\beta}_2) = \langle \varphi(\vec{\beta}_1) | \varphi(\vec{\beta}_2) \rangle \quad (5)$$

and Hamiltonian

$$\mathcal{H}(\vec{\beta}_1, \vec{\beta}_2) = \langle \varphi(\vec{\beta}_1) | \hat{H} | \varphi(\vec{\beta}_2) \rangle \quad (6)$$

kernels. In the evaluation of the density-dependent contribution to the Hamiltonian kernel $\mathcal{H}(\vec{\beta}_1, \vec{\beta}_2)$, we have considered the mixed-density prescription [71]. Perturbative first-order corrections in both the mean value of the proton and neutron numbers have also been included in the calculations [43–47, 69, 71].

In the GHW Eq.(4), the norm kernel $\mathcal{N}(\vec{\beta}_1, \vec{\beta}_2)$ accounts for the non-orthogonality of the HFB states $|\varphi(\vec{\beta})\rangle$. Therefore, the functions $f^\sigma(\vec{\beta})$ cannot be interpreted as probability amplitudes [1]. In order to obtain a probabilistic quantum mechanical interpretation, one introduces the collective wave functions

$$G^\sigma(\vec{\beta}_1) = \int_{\mathcal{D}_{\vec{\beta}_2}} d\vec{\beta}_2 \mathcal{N}^{\frac{1}{2}}(\vec{\beta}_1, \vec{\beta}_2) f^\sigma(\vec{\beta}_2) \quad (7)$$

written in terms of the operational square root of the norm kernel [1, 43, 71]. For the state $|\Psi_{2D-GCM}^\sigma\rangle$ Eq.(3), the dynamical quadrupole and hexadecapole moments $Q_{\lambda 0, 2D-GCM}^\sigma = \langle \Psi_{2D-GCM}^\sigma | \hat{Q}_{\lambda 0} | \Psi_{2D-GCM}^\sigma \rangle$ ($\lambda = 2, 4$) can be computed using the general expressions developed in previous works [43–47]. The deformation parameters $\beta_{\lambda, 2D-GCM}^\sigma$ are related to the moments $Q_{\lambda 0, GCM}^\sigma$ according to Eq.(1). Let us also mention, that the overlaps of operators between different HFB states, required at the GCM level, have been computed using pfaffian techniques [72, 73].

III. DISCUSSION OF THE RESULTS

The results of the calculations for $^{232-268}\text{Ra}$, $^{232-268}\text{Th}$, $^{232-268}\text{U}$ and $^{232-268}\text{Pu}$ are discussed in this section. First, mean-field results will be presented in Sec. III A, while GCM results will be analyzed in Sec. III B.

A. Mean-field calculations

The Gogny-D1S MFPEs obtained for the uranium isotopes $^{232-268}\text{U}$ are depicted in Fig.1, as illustrative examples. Similar results have been obtained for $^{232-268}\text{Ra}$, $^{232-268}\text{Th}$ and $^{232-268}\text{Pu}$. Most of the studied nuclei exhibit prolate ground states. Up to around the mass number $A = 248$, the ground state quadrupole deformation displays variations within the range $0.24 \leq \beta_2 \leq 0.28$. On the other hand, for larger mass numbers those values decrease almost linearly and HFB ground states with $-0.12 \leq \beta_2 \leq 0.0$ are predicted for $^{266, 268}\text{Ra}$, $^{266, 268}\text{Th}$, $^{266, 268}\text{U}$ and ^{268}Pu .

As can be noted from Fig.1, sizable static hexadecapole deformations are predicted around ^{238}U . This agrees well with the conclusions of Ref. [61]. For example, in our calculations we have obtained $\beta_4 = 0.09, 0.13, 0.16$ and 0.17

for ^{238}Ra , ^{238}Th , ^{238}U and ^{238}Pu , respectively. With increasing mass number, the HFB β_4 values decrease steadily up to $\beta_4 = 0$ for ^{248}Ra , ^{250}Th , ^{252}U and ^{254}Pu . For larger mass numbers, as we move closer to the neutron shell closure $N = 184$ [16], a region (i.e., the nuclei $^{250-264}\text{Ra}$, $^{252-264}\text{Th}$, $^{254-264}\text{U}$ and $^{256-266}\text{Pu}$) with $-0.04 \leq \beta_4 \leq -0.02$ is predicted for the considered isotopic chains. Given the small negative β_4 values obtained for those neutron-rich isotopes, and the relatively flat potential energy surface in the β_4 direction, a beyond-mean-field analysis is required to examine the survival of the corresponding static hexadecapole deformations once zero-point quantum fluctuations in the collective (β_2, β_4) -coordinates are taken into account.

The HFB density contour plots corresponding to the ground states ($\beta_2 = 0.28, \beta_4 = 0.16$) and ($\beta_2 = 0.20, \beta_4 = -0.02$) of ^{238}U and ^{256}U are plotted in panels (a) and (c) of Fig.2. In the case of ^{238}U , one observes a typical diamond-like shape corresponding to positive β_4 , while an incipient square-like shape corresponding to a small, negative β_4 value is obtained for ^{256}U . Typical square-like shapes corresponding to a large negative $\beta_4 = -0.4$ value are illustrated for both isotopes in panels (b) and (d) of the figure.

Coming back to the MFPEs displayed in Fig. 1, one realizes that for the lightest U isotopes, the excitation energy of oblate configurations is large and, therefore, their contribution to the ground state dynamics can be safely neglected. We have checked this point by performing 2D-GCM calculations for the isotopes $^{232-240}\text{U}$ in which only configurations with $\beta_2 \geq 0$ have been included in the 2D-GCM state Eq.(3). However, the structural evolution of the MFPEs in Fig.1 also reveals that as we move to more neutron-rich sectors of the considered isotopic chains, oblate configurations decrease their excitation energy and, at least for some of the considered nuclei, there is a pronounced competition between different intrinsic (quadrupole and/or hexadecapole) shapes. For instance, in the case of ^{260}U and ^{264}U the oblate configurations at $(\beta_2 = -0.14, \beta_4 = 0.04)$ and $(\beta_2 = -0.12, \beta_4 = 0.02)$ lie 1.50 and 0.38 MeV above the corresponding ground states. Moreover, the MFPEs obtained for the oblate-deformed isotopes ^{266}U and ^{268}U exhibit a soft behavior along the quadrupole direction. Similar results, have been obtained for Ra, Th and Pu nuclei.

In Fig.1 we also observe that, for several of the studied nuclei (i.e., $^{232-256}\text{U}$), the corresponding MFPE displays an energy valley that, in the neighborhood of the absolute minimum, roughly follows a straight line with positive slope in the (β_2, β_4) -plane for prolate deformations. This straight line corresponds to the direction labeled as A in the figure. Along this direction A, the hexadecapole deformation β_4 exhibits a linear behavior $\beta_4 = a_A \beta_2 + b_A$ as a function of β_2 . The line B, defines the direction perpendicular to A. Along the direction B, β_4 also exhibits a linear behavior $\beta_4 = -(1/a_A)\beta_2 + b_B$. For each nucleus, we have approximately fitted a_A , b_A and b_B using configurations around the absolute minimum of

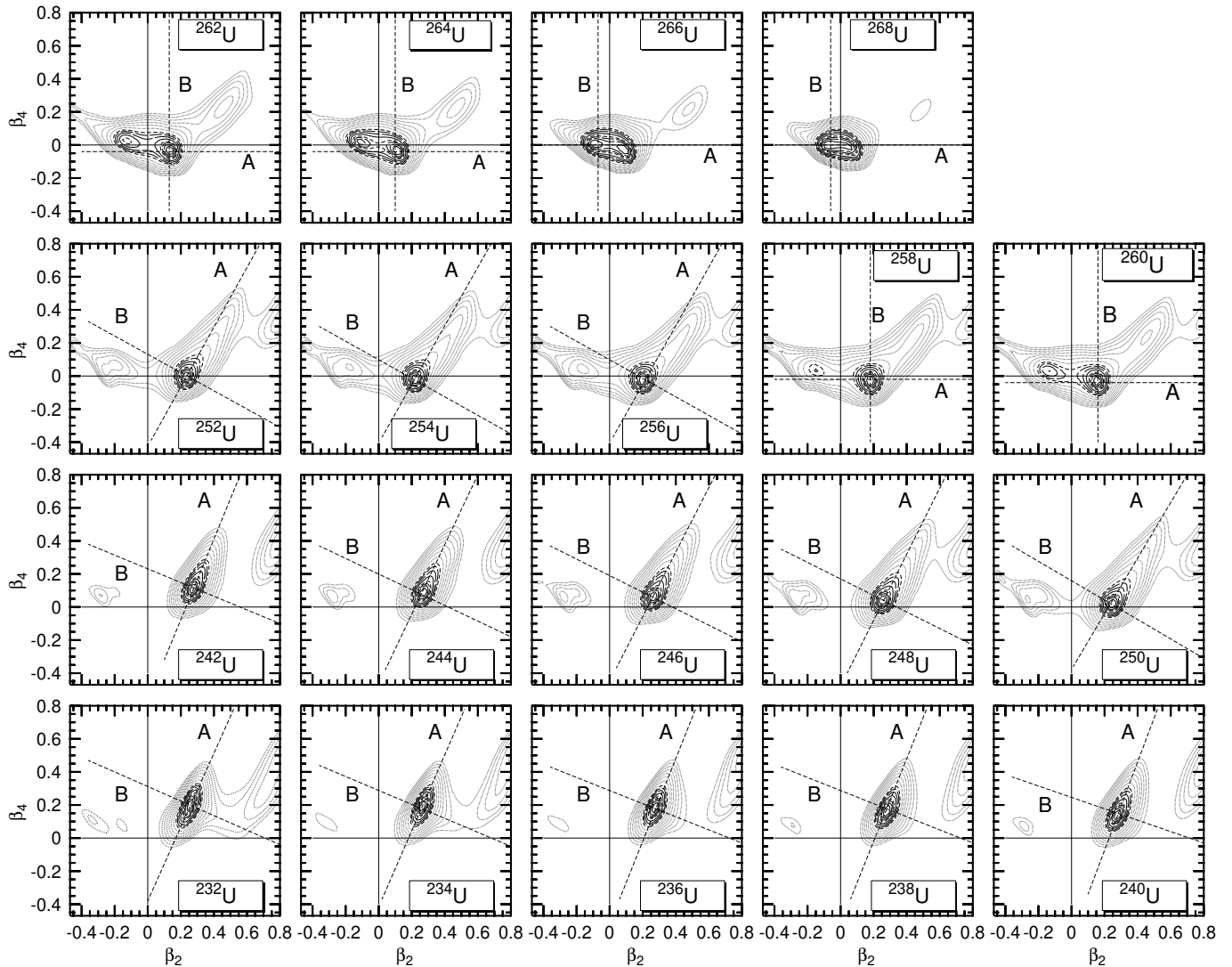


FIG. 1. MFPEs computed with the Gogny-D1S EDF for the isotopes $^{232-268}\text{U}$. Contour lines extend from 0.25 MeV up to 1 MeV above the ground state energy in steps of 0.25 MeV in the ascending sequence full, long-dashed, medium-dashed and short-dashed. The next contours following the same sequence correspond to energies from 1.5 MeV up to 3 MeV above the ground state in steps of 0.5 MeV. From there on, dotted contour lines are drawn in steps of 1 MeV. For each nucleus, the two perpendicular dotted lines A and B are drawn along the principal axes of the parabola that approximates the HFB energy around the absolute minimum of the MFPEs. A vertical full line is drawn to signal the $\beta_2 = 0$ line whereas a full horizontal line is drawn to signal the $\beta_4 = 0$ line. For more details, see the main text.

the MFPEs. For example, in the case of ^{238}U the directions A and B are parameterized as $\beta_4 = 2.50\beta_2 - 0.52$ and $\beta_4 = -0.40\beta_2 + 0.29$, respectively.

The energy E_{HFB} , as a function of the deformation parameter β_2 , along the directions A and B is depicted in Fig.3 for ^{238}U . As can be seen, it exhibits a parabolic behavior in both cases. Thus, as indicated in the caption of Fig.1, the directions A and B are nothing else than the principal axes of the two-dimensional parabola that approximates the HFB energy around the absolute minimum of the MFPEs.

The tilted parabolic behavior of E_{HFB} already described implies, that 1D-GCM calculations using β_2 or

β_4 as single generating coordinates roughly explore the same configurations around the minimum of the MFPEs [59]. Thus, for several of the studied U but also Ra, Th and Pu isotopes, the quadrupole and hexadecapole degrees of freedom cannot be decoupled and full-fledged 2D-GCM calculations must be carried out. As discussed below, a cheaper alternative to the 2D-GCM calculation is to perform 1D-GCM calculations along paths A and B discussed above. Note that, in particular, ^{238}U belongs to this coupled regime. This is at variance with the rather weak quadrupole-octupole coupling, observed in previous studies [43–47]. The exceptions in our calculations are neutron-rich isotopes, such as $^{258-268}\text{U}$, for which

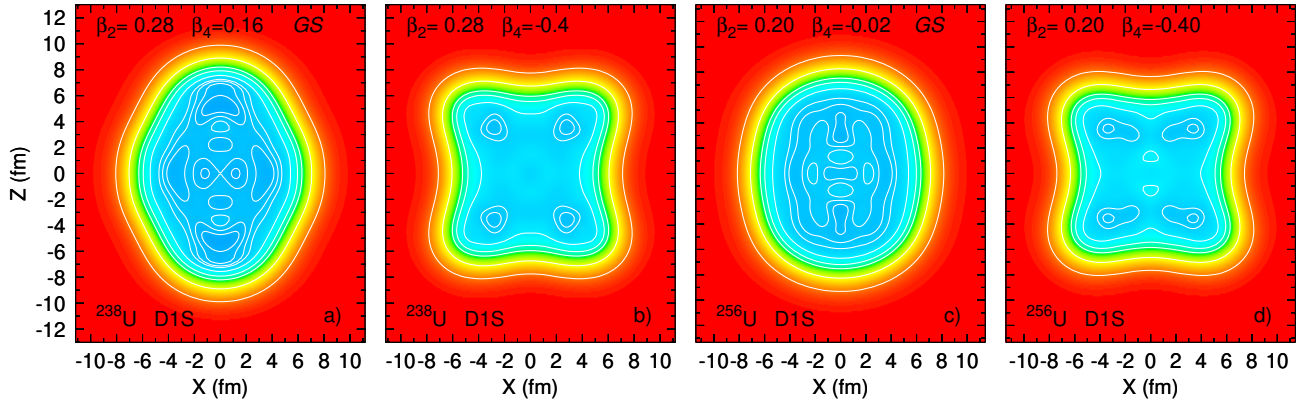


FIG. 2. (Color online) Mean-field density contour plots for the isotopes ^{238}U [panels a) and b)] and ^{256}U [panels c) and d)]. The ground state (GS) in ^{238}U [panel a)] corresponds to $\beta_2=0.28$ and $\beta_4=0.16$, while the GS in ^{256}U [panel c)] corresponds to $\beta_2=0.20$ and $\beta_4=-0.02$. Typical square-like shapes corresponding to a large negative $\beta_4=-0.4$ deformation parameter are plotted in panels b) and d). Densities are in units of fm^{-3} and contour lines are drawn at 0.01, 0.05, 0.10, 0.12, 0.14, 0.15, 0.16 and 0.17 fm^{-3} . Results have been obtained with the Gogny-D1S EDF.

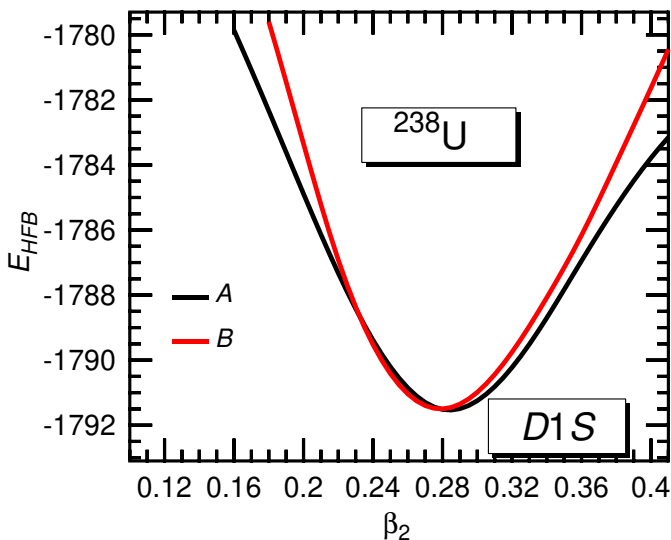


FIG. 3. (Color online) HFB energy, as a function of the deformation parameter β_2 , along the directions A ($\beta_4 = 2.50\beta_2 - 0.52$) and B ($\beta_4 = -0.40\beta_2 + 0.29$) for the nucleus ^{238}U . Results have been obtained with the Gogny-D1S EDF. For more details, see the main text.

the directions A and B run parallel to the quadrupole and hexadecapole axes, respectively. In those cases, one might anticipate a weak coupling of the quadrupole and hexadecapole degrees of freedom.

B. GCM calculations

The ground state collective wave functions $G^{\sigma=1}(\vec{\beta})$ obtained for $^{232-268}\text{U}$ are shown in Fig. 4, as illustrative examples. It becomes apparent from the figure that for $^{232-256}\text{U}$, those wave functions are well approximated by a Gaussian with principal directions aligned along the directions A and B, already discussed in Sec. III A. On the other hand, for $^{258-268}\text{U}$ they align parallel to the β_2 axis and, therefore, in those isotopes the (β_2, β_4) -coupling is rather weak. This is similar to the situation encountered in previous dynamical studies (see, for example, [47]) in which the quadrupole-octupole coupling has been shown to be rather weak and the corresponding ground state collective wave functions align along the octupole axis. Regardless of their particular alignment, the maxima of the collective wave functions in Fig. 4 correspond to β_2 and β_4 values close to the absolute minima of the MF-PESs.

For the other isotopic chains the nuclei signaling the transition from coupled to uncoupled (β_2, β_4) regime also correspond to neutron number 166-168.

The previous results agree well with the structural evolution of the MF-PESs and corroborate, from a dynamical point of view, the transition from a (β_2, β_4) -coupled to a (β_2, β_4) -decoupled regime in the 2D-GCM ground states of the studied nuclei with increasing mass number. Furthermore, they corroborate the relevance [59] of collective deformations along the A and B directions as alternative generating coordinates in GCM calculations for the considered Ra, Th, U and Pu nuclei. With this in mind, we

have also performed 1D-GCM calculations along those directions for all the studied isotopes.

The ground state quadrupole $\beta_{2,2D-GCM}^{\sigma=1}$ and hexadecapole $\beta_{4,2D-GCM}^{\sigma=1}$ deformation parameters obtained for $^{232-268}\text{Ra}$, $^{232-268}\text{Th}$, $^{232-268}\text{U}$ and $^{232-268}\text{Pu}$ are depicted in panels (a)-(d) and (e)-(h) of Fig. 5, respectively. Their values are rather close to the ones obtained at the HFB level. In particular, the $\beta_{2,GCM}^{\sigma=1}$ deformations slightly increase up to 0.26, 0.27, 0.29 and 0.29 in ^{236}Ra , ^{236}Th , ^{238}U and ^{240}Pu , respectively, while for larger mass numbers they decrease until 2D-GCM ground states with $-0.06 \leq \beta_{2,2D-GCM}^{\sigma=1} \leq 0.00$ are obtained for $^{262-268}\text{Ra}$, $^{264-268}\text{Th}$, $^{266-268}\text{U}$ and $^{266-268}\text{Pu}$.

As can be seen from panels (e)-(h), sizable dynamical hexadecapole $\beta_{4,GCM}^{\sigma=1}$ values are predicted around ^{238}U [61]. For example, we have obtained $\beta_{4,GCM}^{\sigma=1} = 0.10, 0.13, 0.16$ and 0.18 for ^{238}Ra , ^{238}Th , ^{238}U and ^{238}Pu , respectively. Furthermore, our 2D-GCM calculations corroborate the dynamical survival of regions (i.e., the nuclei $^{250-260}\text{Ra}$, $^{252-262}\text{Th}$, $^{254-264}\text{U}$ and $^{256-264}\text{Pu}$) with small negative hexadecapole deformations $-0.034 \leq \beta_{4,GCM}^{\sigma=1} \leq -0.014$ in each of the considered isotopic chains, just below the neutron magic number $N = 184$ [59, 62, 63].

In panels (i)-(l) of Fig. 5, we have plotted the 2D-GCM correlation energies defined as the difference

$$E_{\text{Corr},2D-GCM} = E_{\text{HFB},gs} - E^{\sigma=1} \quad (8)$$

between the HFB $E_{\text{HFB},gs}$ and 2D-GCM $E^{\sigma=1}$ ground state energies. For the studied nuclei, $1.42 \text{ MeV} \leq E_{\text{Corr},2D-GCM} \leq 1.72 \text{ MeV}$. The range of variation of the correlation energies (0.3 MeV) is comparable to typical values of the rms for the binding energy in Gogny-like mass tables [60, 65]. Therefore, the correlation energies $E_{\text{Corr},2D-GCM}$ should be taken into account in future fitting protocols of the Gogny-EDF.

A more quantitative measure of the role of hexadecapole deformation and its coupling to the quadrupole degree of freedom in the ground state dynamics, can be obtained from the comparison with correlation energies $E_{\text{Corr},1D-GCM}^{Q2}$ resulting from 1D-GCM calculations based on the ansatz

$$|\Psi^\sigma\rangle = \int_{\mathcal{D}_2} d\beta_2 f^\sigma(\beta_2) |\varphi(\beta_2)\rangle \quad (9)$$

in which, the basis states $|\varphi(\beta_2)\rangle$ are obtained via β_2 -constrained HFB calculations in the domain $\mathcal{D}_2 = \left\{ \beta_2 \in [-0.4, 1.2] \right\}$ with the step size $\delta\beta_2 = 0.01$. For the studied nuclei, we have obtained $0.45 \text{ MeV} \leq E_{\text{Corr},1D-GCM}^{Q2} \leq 0.98 \text{ MeV}$. Thus, in going from the (quadrupole) 1D- to the (quadrupole-hexadecapole) 2D-GCM, we gain an additional correlation energy $0.74 \text{ MeV} \leq \delta E_{\text{Corr}} \leq 0.97 \text{ MeV}$ similar to the quadrupole correlation energy itself. These results, and the ones obtained in previous studies [43–47, 59], suggest a slow convergence of the nuclear correlation energy with respect to the (even and/or

odd) shape multipole moments included within the GCM framework and deserve further attention in future work.

Given the relevance of the directions A and B, we have also carried out 1D-GCM calculations along those directions. Within this context, we have considered the ansatz

$$|\Psi_A^\sigma\rangle = \int_{\mathcal{D}_A} d\beta_2 f_A^\sigma(\beta_2) |\varphi(\beta_2)\rangle \quad (10)$$

where the integration domain reads $\mathcal{D}_A = \left\{ \beta_2 \in [-0.4, 1.2]; \beta_4 = a_A \beta_2 + b_A \right\}$. Another set of calculations resorted to a similar ansatz

$$|\Psi_B^\sigma\rangle = \int_{\mathcal{D}_B} d\beta_2 f_B^\sigma(\beta_2) |\varphi(\beta_2)\rangle \quad (11)$$

with the domain $\mathcal{D}_B = \left\{ \beta_2 \in [-0.4, 1.2]; \beta_4 = -(1/a_A)\beta_2 + b_B \right\}$. In both sets, we have employed the step $\delta\beta_2 = 0.01$. For each nucleus, the parameters a_A , b_A and b_B have been fitted along the lines already discussed in Sec. III A. As can be seen from panels (a)-(d) and (e)-(h) of Fig. 5, the quadrupole and hexadecapole deformations corresponding to the 1D- and 2D-GCM ground states $|\Psi_A^{\sigma=1}\rangle$, $|\Psi_B^{\sigma=1}\rangle$ and $|\Psi_{2D-GCM}^{\sigma=1}\rangle$ are rather similar.

In panels (i)-(l) of Fig. 5, we have also included the 1D-GCM correlation energies $E_{\text{Corr},1D-GCM}^A$ and $E_{\text{Corr},1D-GCM}^B$. In most cases, those energies are rather similar and, as expected, the A path results compare well with the corresponding quadrupole $E_{\text{Corr},1D-GCM}^{Q2}$ values. Moreover, the sum $E_{\text{Corr},1D-GCM}^A + E_{\text{Corr},1D-GCM}^B$ approximates $E_{\text{Corr},2D-GCM}$ reasonably well. Let us also stress, that in going from 1D-GCM calculations along the directions A and B to the 2D-GCM ones we gain the additional correlation energies $0.74 \text{ MeV} \leq \delta E_{\text{Corr}} \leq 0.81 \text{ MeV}$ and $0.66 \text{ MeV} \leq \delta E_{\text{Corr}} \leq 0.94 \text{ MeV}$, respectively. Once more, these results point towards the key role of the (β_2, β_4) dynamical zero-point fluctuations in the ground states of the considered nuclei.

The collective wave functions $G^{\sigma=2}(\vec{\beta})$ corresponding to the first excited states in $^{232-268}\text{U}$ are shown in Fig. 6. For the isotopes $^{232-236}\text{U}$ and $^{240-252}\text{U}$ (^{238}U and $^{254,256}\text{U}$) they correspond to phonons aligned along the tilted direction A (B). In such phonons the quadrupole and hexadecapole degrees of freedom are coupled. On the other hand, the wave functions $G^{\sigma=2}(\vec{\beta})$ in $^{258-268}\text{U}$ align parallel to the quadrupole axis. For both $^{258-262}\text{U}$, the collective amplitude mainly concentrates on the oblate minimum and corresponds to a shape isomeric excited state, while for $^{264-268}\text{U}$ the first excited state slowly evolves from the oblate configuration to a pure two-phonon quadrupole vibration.

The analysis of the collective amplitudes $G^{\sigma=3}(\vec{\beta})$, associated with the second excited states, shown in Fig. 7, reveals a quite rich casuistic. The amplitudes in the isotopes $^{232-236}\text{U}$ correspond to the second vibration phonon along direction A. In the case of ^{238}U the first excited state corresponds to a phonon along the direction

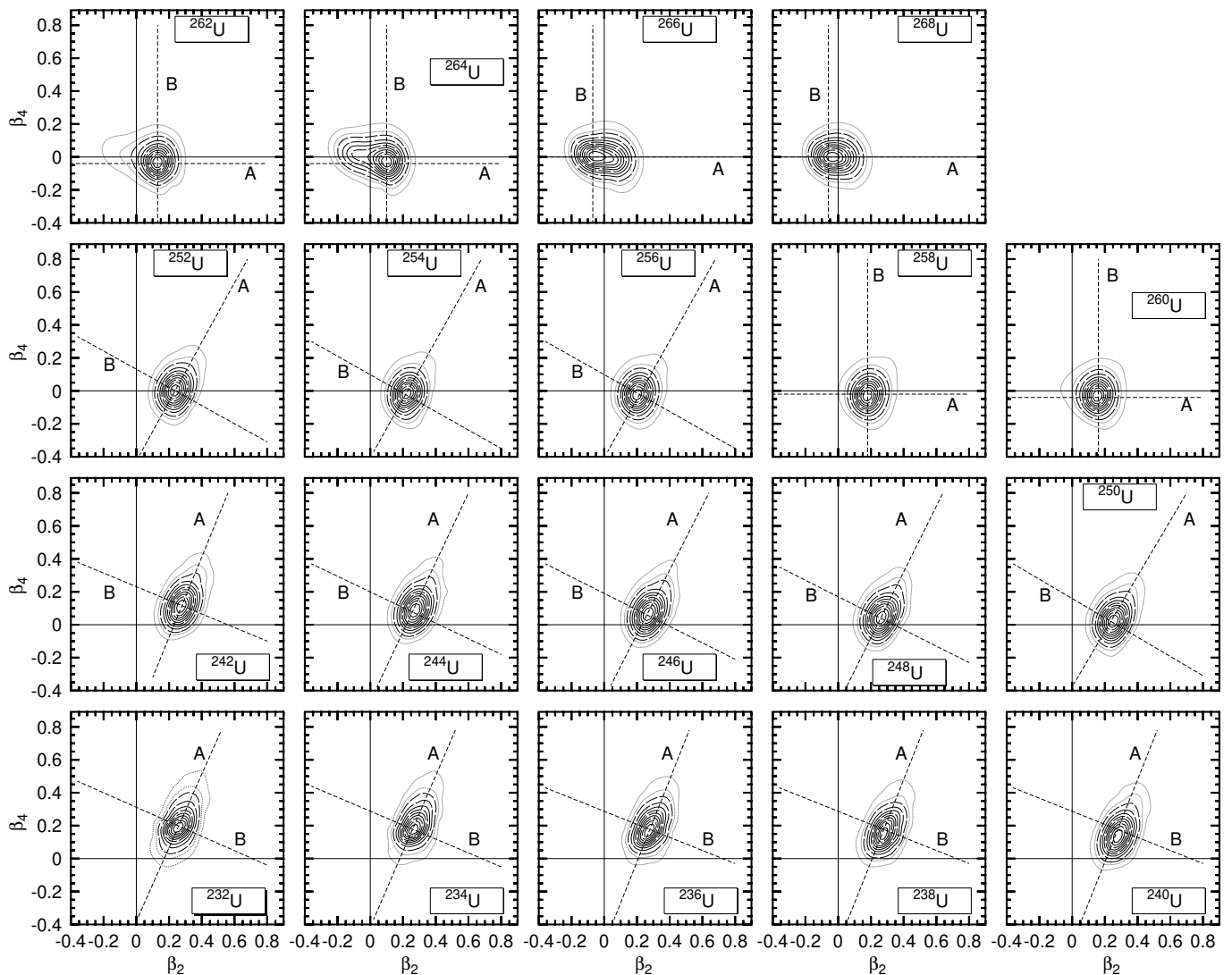


FIG. 4. Collective wave functions Eq.(7) corresponding to the ground states of the nuclei $^{232-268}\text{U}$. The succession of solid, long dashed and short dashed contour lines starts at 90% of the maximum value up to 10% of it. The two dotted-line contours correspond to the tail of the amplitude (5% and 1% of the maximum value). For each nucleus, the two perpendicular dotted lines A and B are drawn along the principal axes of the parabola that approximates the HFB energy around the absolute minimum of the MFPEs and are the same as in Fig.1. A vertical full line is drawn to signal the $\beta_2 = 0$ line whereas a full horizontal line is drawn to signal the $\beta_4 = 0$ line. Results have been obtained with the Gogny-D1S EDF. For more details, see the main text.

B, while the second excited state represents a phonon along the direction A. For the isotopes $^{240-252}\text{U}$ the second excited state corresponds to a phonon along the B direction. However, for $^{254-260}\text{U}$ the second excited state corresponds to a single phonon along the A direction, whereas for $^{262-268}\text{U}$ two phonon excitations along the A direction are observed. As a general conclusion, not only for the ground but also for the first and second excited states of the studied nuclei, our calculations predict a transition from a (β_2, β_4) -coupled to a (β_2, β_4) -decoupled regime with increasing mass number.

The analysis of all the collective amplitudes discussed above reveal that while the ground state can be well described by two 1D-GCM calculations along the A and B

directions, the situation becomes more intricate as one considers higher excited states (consider, for instance, $^{250-252}\text{U}$) and there are some specific cases where the 2D-GCM calculation is required. Unfortunately, there is not a clear trend with neutron number and our recommendation is to perform the full fledged 2D-GCM calculation when the properties of excited states are required.

The 2D-GCM quadrupole deformations $\beta_{2,2D-GCM}^{\sigma=2}$ and $\beta_{2,2D-GCM}^{\sigma=3}$ obtained for $^{232-268}\text{Ra}$, $^{232-268}\text{Th}$, $^{232-268}\text{U}$ and $^{232-268}\text{Pu}$ are plotted in panels (a)-(d) of Fig.8. The first excited states of $^{232-252}\text{Ra}$, $^{232-254}\text{Th}$, $^{232-256}\text{U}$ and $^{232-258}\text{Pu}$ are prolate deformed. At variance with their ground states (see, Fig.5), the first

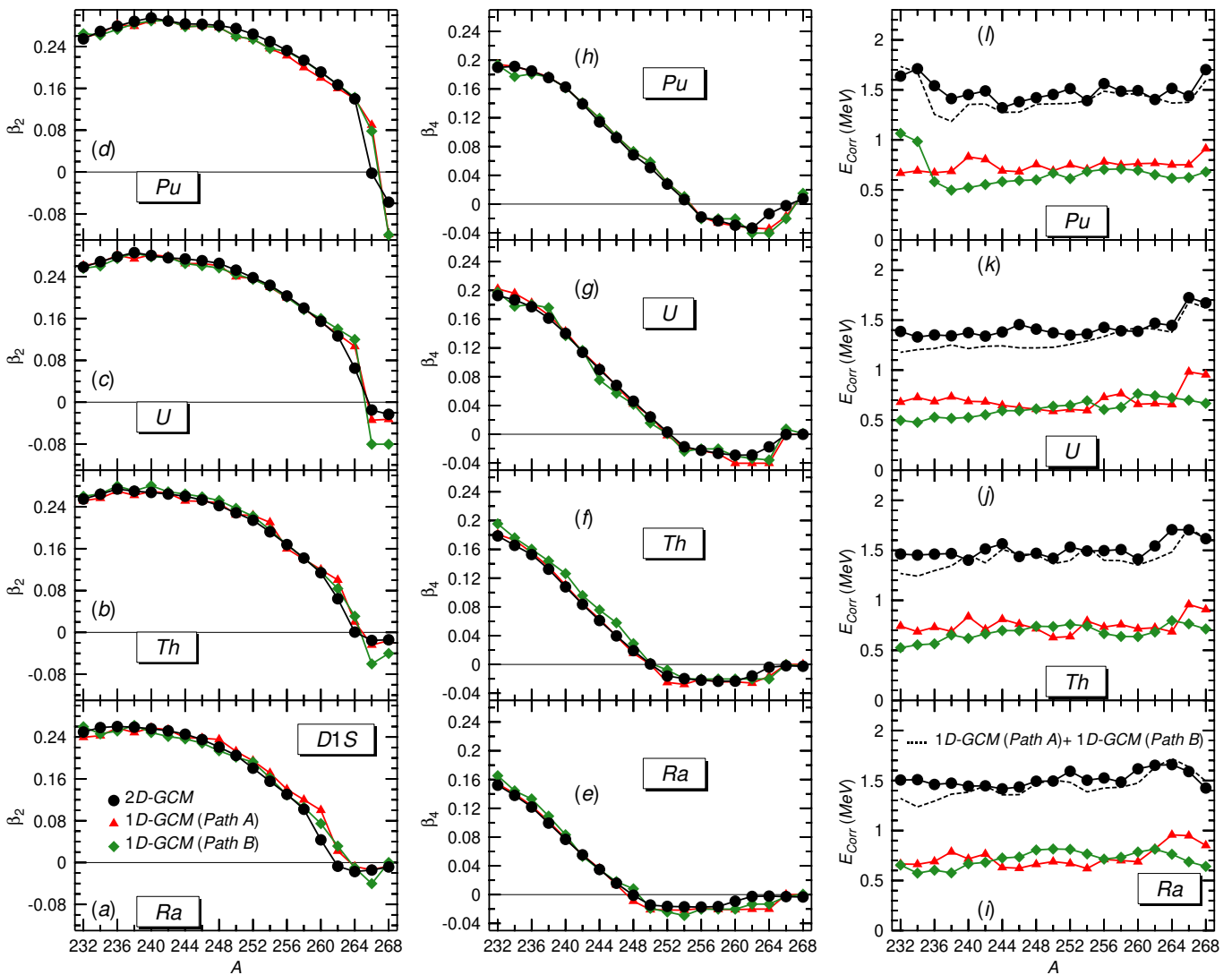


FIG. 5. (Color online) 2D-GCM ground state quadrupole β_2 [panels (a)-(d)] and hexadecapole β_4 [panels (e)-(h)] deformation parameters for $^{232-268}\text{Ra}$, $^{232-268}\text{Th}$, $^{232-268}\text{U}$ and $^{232-268}\text{Pu}$. The 2D-GCM correlation energies $E_{\text{Corr},2D-GCM}$ obtained for those nuclei are depicted in panels (i)-(l). Quadrupole and hexadecapole deformations as well as correlation energies obtained in 1D-GCM calculations along the directions A and B are also included in the plots. The dotted lines in panels (i)-(l) correspond to the sum of 1D-GCM correlation energies along the directions A and B. Results have been obtained with the Gogny-D1S EDF. For more details, see the main text.

excited states of $^{254-260}\text{Ra}$, $^{256-262}\text{Th}$, $^{258-264}\text{U}$ and $^{260-264}\text{Pu}$ exhibit oblate deformations within the range $-0.14 \leq \beta_{2,2D-GCM}^{\sigma=2} \leq -0.04$. As already discussed in Sec. III A (see, Fig 1), for the more neutron-rich sectors in each of the studied isotopic chains, the MFPEs exhibit soft features as well as a more pronounced competition between low-lying configurations based on different intrinsic shapes. From a dynamical point of view, both the 2D-GCM shape transitions in $^{254-260}\text{Ra}$, $^{256-262}\text{Th}$, $^{258-264}\text{U}$ and $^{260-264}\text{Pu}$ and the $\beta_{2,2D-GCM}^{\sigma=2}$ values obtained for heavier isotopes, reflect this enhanced shape coexistence and result from the structure of the corresponding collective wave functions $G^{\sigma=2}(\vec{\beta})$ in Fig. 6. Similar arguments hold for the $\beta_{2,2D-GCM}^{\sigma=3}$ deforma-

tions resulting from the structure of the wave functions $G^{\sigma=3}(\vec{\beta})$ in Fig. 7. Note that, the sudden jump to $\beta_{2,2D-GCM}^{\sigma=3} < 0$ values observed in $^{250-252}\text{Ra}$ and ^{254}Th results from the concentration of a significant portion of the corresponding collective $G^{\sigma=3}(\vec{\beta})$ strengths on the oblate side.

The hexadecapole deformations $\beta_{4,2D-GCM}^{\sigma=2}$ and $\beta_{4,2D-GCM}^{\sigma=3}$ corresponding to the first and second excited states in $^{232-268}\text{Ra}$, $^{232-268}\text{Th}$, $^{232-268}\text{U}$ and $^{232-268}\text{Pu}$ are shown in panels (e)-(h) of Fig. 8. In our calculations, we have obtained $\beta_{4,GCM}^{\sigma=2} = 0.09, 0.17, 0.17$ and 0.17 ($\beta_{4,GCM}^{\sigma=3} = 0.16, 0.14, 0.18$ and 0.19) for the first (second) excited states in ^{238}Ra , ^{238}Th , ^{238}U and ^{238}Pu . Therefore, not only for the ground but also for the first two

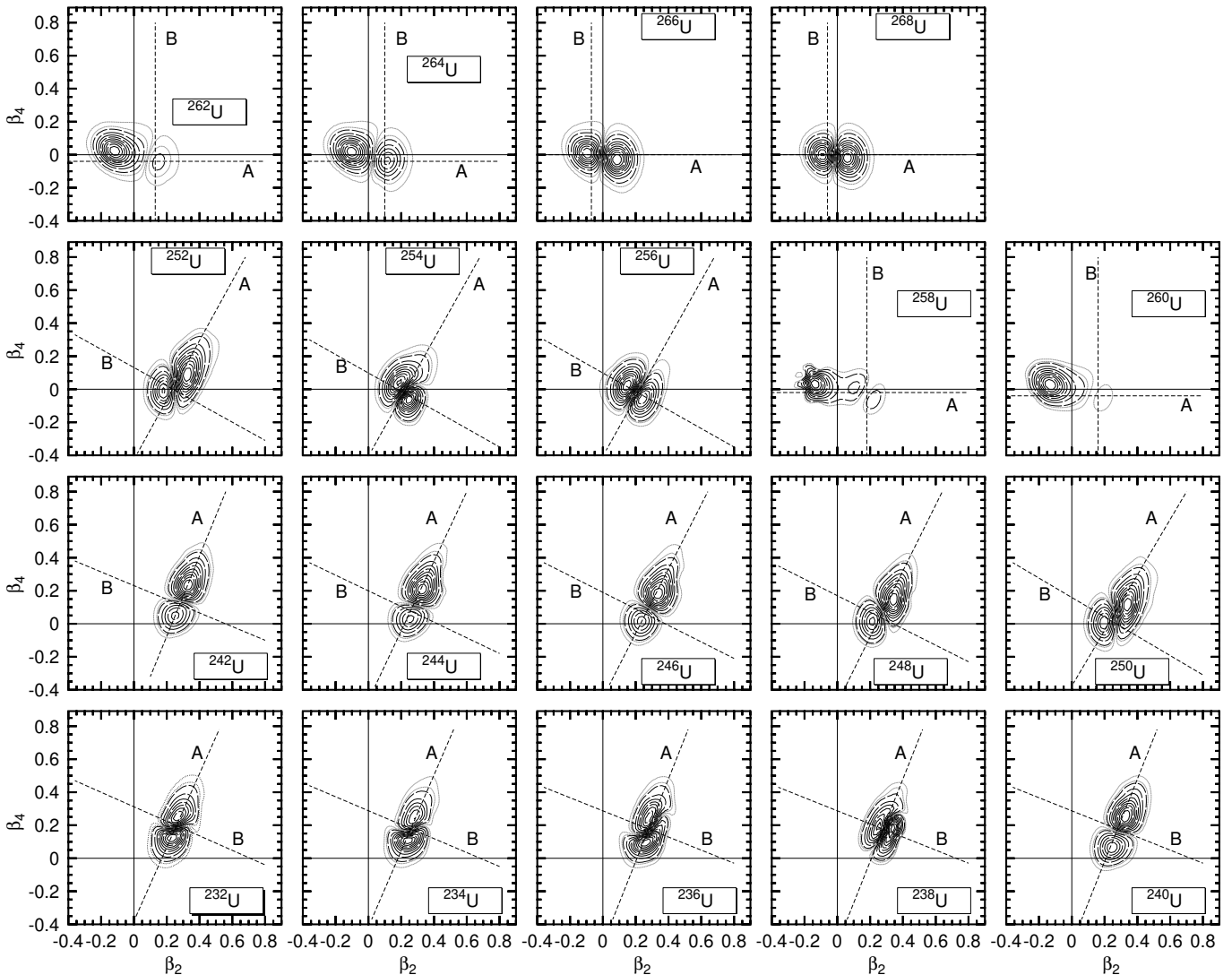


FIG. 6. The same as in Fig. 4 but for the first excited 2D-GCM states of the nuclei $^{232-268}\text{U}$.

excited states of nuclei around ^{238}U hexadecapole deformations play a significant role [61]. For Ra isotopes, the $\beta_{4,2D-GCM}^{\sigma=2}$ deformations exhibit a smooth decrease up to the mass number $A = 252$. On the other hand, in the case of Th, U and Pu nuclei, those $\beta_{4,2D-GCM}^{\sigma=2}$ values display a steady decrease after reaching a maximum for $A = 240, 242$. At variance with their ground states, the first excited states of $^{254-260}\text{Ra}$, $^{256-262}\text{Th}$, $^{258-264}\text{U}$ and $^{260-264}\text{Pu}$ correspond to diamond-like shapes. Note that these are precisely the same nuclei, for which quadrupole transitions are observed in panels (a)-(d) of the figure. On the other hand, for heavier isotopes weakly deformed square-like shapes are predicted. Besides their overall decreasing trend, the deformations $\beta_{4,2D-GCM}^{\sigma=3}$ also exhibit a transition to a weakly hexadecapole deformed regime around $A = 254 - 258$. We stress, once more, that these features reflect the enhanced shape coexistence in the more neutron-rich sectors of the studied isotopic chains.

Finally, in panels (i)-(l) of Fig. 8 we have depicted the

excitation energies $\Delta E^{\sigma=2}$ and $\Delta E^{\sigma=3}$. The most striking feature observed in those panels is the pronounced reduction of the excitation energies for the most neutron-rich Ra, Th, U and Pu isotopes with an almost parabolic behavior around their global minima for ^{260}Ra , ^{262}Th , ^{264}U and ^{266}Pu . In particular, we have obtained $\Delta E^{\sigma=2} = 340, 360, 250, 91$ KeV and $\Delta E^{\sigma=3} = 1.46, 1.33, 1.13$ and 1.11 MeV. It is precisely the enhanced shape coexistence around those nuclei, what brings the excitation energies $\Delta E^{\sigma=2}$ and $\Delta E^{\sigma=3}$ to such low values as compared with lighter nuclei.

IV. CONCLUSIONS

In this work, we have addressed the emergence and stability of static hexadecapole deformation effects as well as the impact of the dynamical quadrupole-hexadecapole configuration mixing on a selected set of radium, tho-

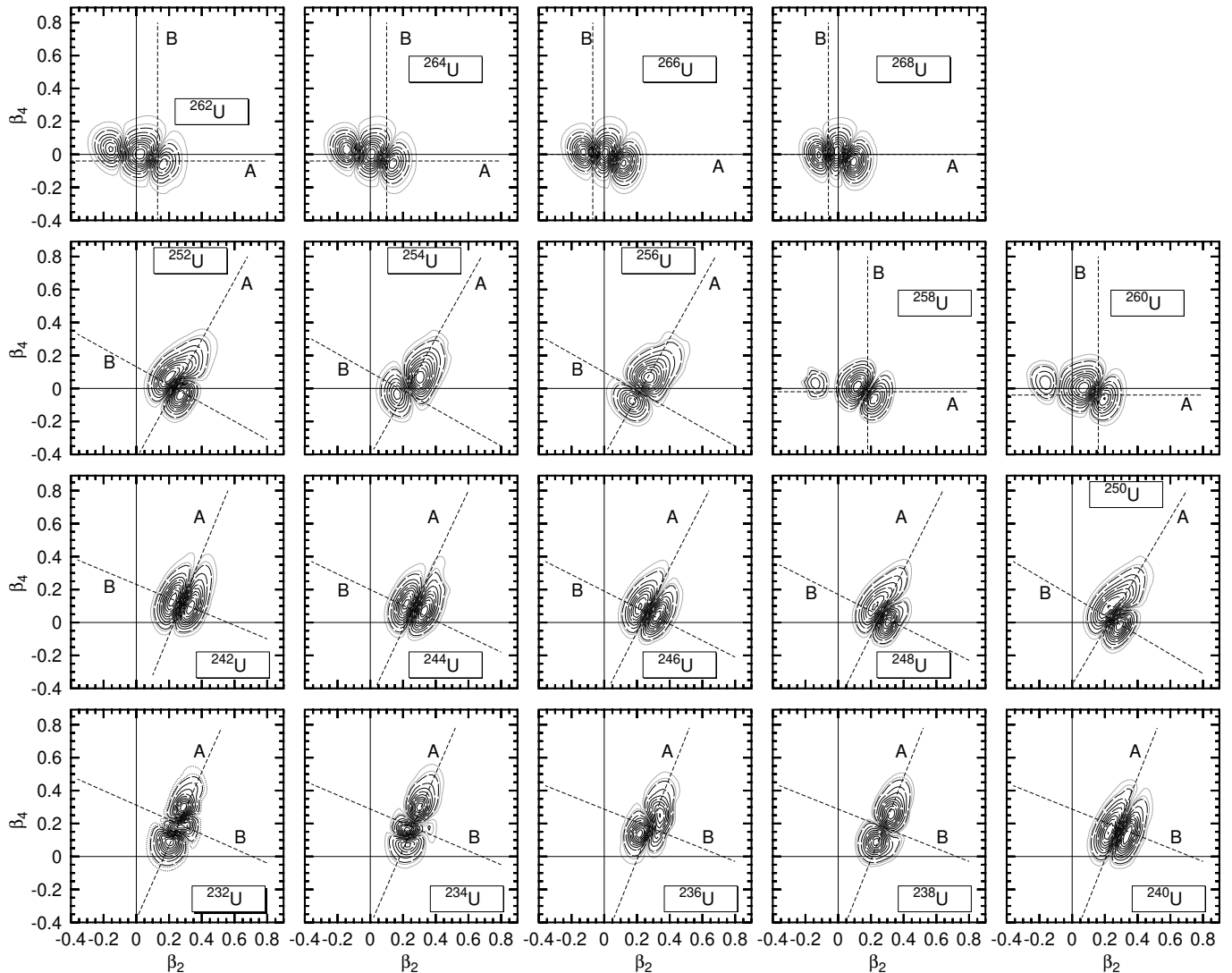


FIG. 7. The same as in Fig. 4 but for the second excited 2D-GCM states of the nuclei $^{232-268}\text{U}$.

rium, uranium and plutonium isotopes covering the mass numbers $232 \leq A \leq 268$. To this end, we have resorted to the (β_2, β_4) -constrained Gogny-D1S HFB approximation, followed by beyond-mean-field 2D-GCM calculations with the deformation parameters β_2 and β_4 as generating coordinates.

From the results of both HFB and 2D-GCM calculations, we conclude that diamond-like shapes play a prominent role around ^{238}U . In particular, sizable static and dynamic hexadecapole deformations are found not only for ground but also for the first two excited states of nuclei in the neighborhood of ^{238}U . This agrees well with the conclusions extracted from the analysis of hydrodynamic simulations of the quark-gluon plasma at the BNL Relativistic Heavy Ion Collider (RHIC) [61]. In agreement with a previous HFB study [59] and the polar gap model [62, 63], for each of the studied isotopic chains, our results corroborate the dynamical survival of a region characterized by square-like shapes (with asso-

ciated weak hexadecapole deformations) just below the neutron magic number $N = 184$.

We have carried out a detailed analysis of the collective wave functions associated with both ground and excited states. We conclude that, with increasing mass number, a transition from a regime in which the quadrupole and hexadecapole degrees of freedom are interwoven to a regime in which they are decoupled, takes place for the studied isotopic chains. This is accompanied by an enhanced quadrupole shape coexistence in the more neutron-rich sectors of those chains. This enhanced quadrupole shape coexistence, reflected in the structure of the corresponding collective wave functions, leads to low values of the excitation energies for ^{260}Ra , ^{262}Th , ^{264}U and ^{266}Pu .

We have obtained 2D-GCM ground state correlation energies which are of the same order of magnitude as the rms for the binding energy in Gogny-like mass tables [60, 65]. Therefore, those ground state correla-

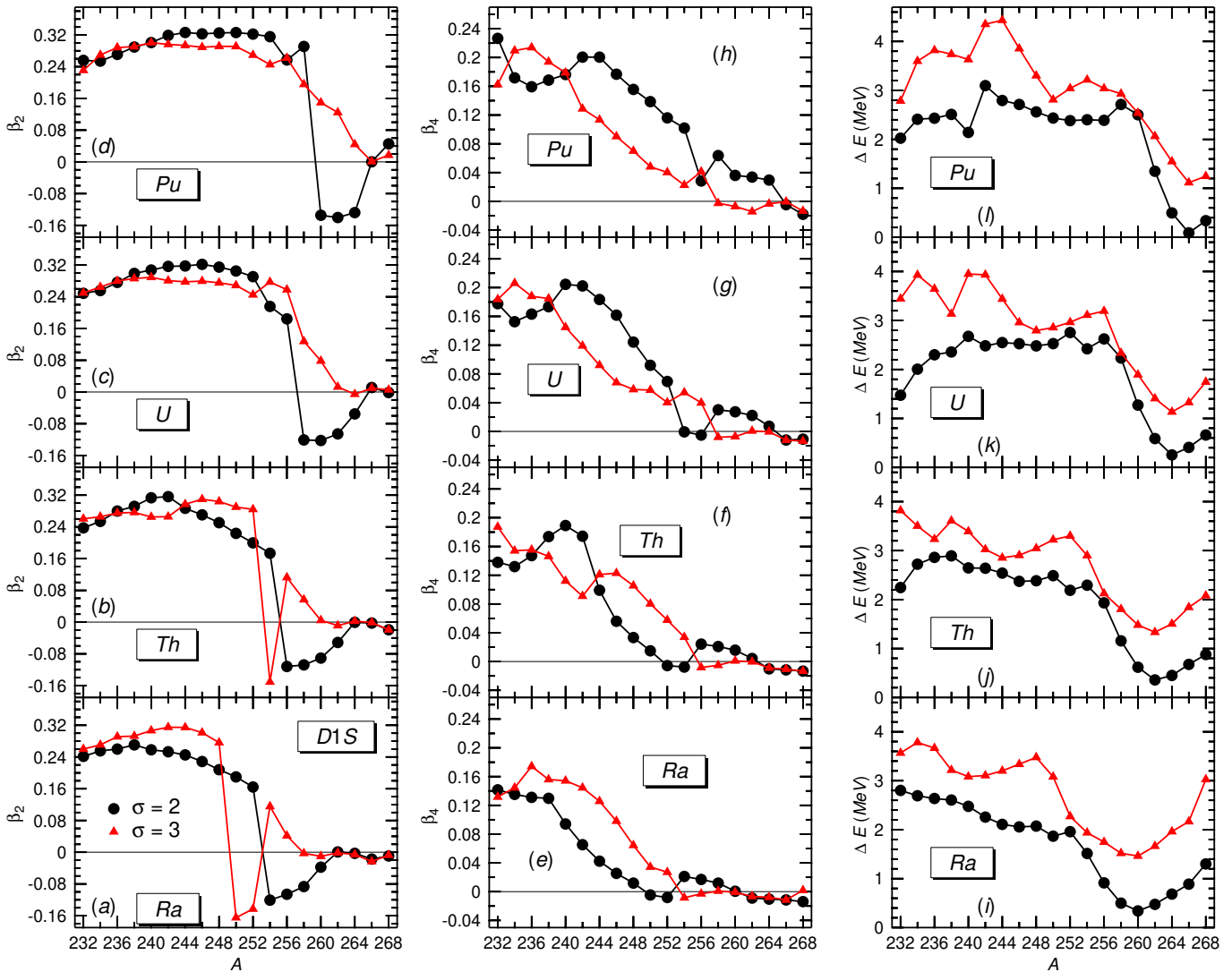


FIG. 8. (Color online) 2D-GCM first ($\sigma = 2$) and second ($\sigma = 3$) excited states quadrupole β_2 [panels (a)-(d)] and hexadecapole β_4 [panels (e)-(h)] deformation parameters for $^{232-268}\text{Ra}$, $^{232-268}\text{Th}$, $^{232-268}\text{U}$ and $^{232-268}\text{Pu}$. The excitation energies $\Delta E^{\sigma=2}$ and $\Delta E^{\sigma=3}$ corresponding to those states are depicted in panels (i)-(l). Results have been obtained with the Gogny-D1S EDF. For more details, see the main text.

tion energies including the hexadecapole degree of freedom should also be considered in future parametrizations of the Gogny-EDF. From the comparison of the 2D-GCM and (quadrupole) 1D-GCM correlation energies we conclude, that the inclusion of hexadecapole deformation in the ground state dynamics leads to an additional (correlation) energy gain which is comparable to the quadrupole correlation energy itself. Similar conclusions can be extracted from the comparison of 2D-GCM correlation energies with the ones obtained in 1D-GCM calculations based on generating coordinates essentially determined by the principal axes of the parabola approximating the energy around the HFB equilibrium configuration. Furthermore, the results of this and previous studies [43–47, 59] point towards a slow convergence of

the correlation energy with respect to the (even and/or odd) shape multipole moments included within the GCM ansatz, and deserve attention in future works.

ACKNOWLEDGMENTS

The work of LMR is supported by Spanish Agencia Estatal de Investigación (AEI) of the Ministry of Science and Innovation under Grant No. PID2021-127890NB-I00. The work of R. Rodríguez-Guzmán was partially supported through the grant PID2022-136228NB-C22 funded by MCIN/AEI/10.13039/501100011033/FEDER, UE and "ERDF A way of making Europe".

-
- [1] P. Ring and P. Schuck, *The Nuclear Many-Body Problem* (Springer, Berlin-Heidelberg-New York) (1980).
- [2] P. Sarriguren, R. Rodríguez-Guzmán and L. M. Robledo, *Phys. Rev. C* **77**, 064322 (2008).
- [3] L. M. Robledo, R. Rodríguez-Guzmán and P. Sarriguren, *J. Phys. G: Nucl. Part. Phys.* **36**, 115104 (2009).
- [4] R. Rodríguez-Guzmán, P. Sarriguren, L. M. Robledo and J. E. García-Ramos, *Phys. Rev. C* **84**, 024310 (2010).
- [5] T. Niksic, Z. P. Li, D. Vretenar, L. Próchniak, J. Meng and P. Ring, *Phys. Rev. C* **79**, 034303 (2009)
- [6] Y. Fu, H. Mei, J. Xiang, Z. P. Li, J. M. Mao and J. Meng, *Phys. Rev. C* **87**, 054305 (2013).
- [7] K. Nomura, T. Niksic and D. Vretenar, *Phys. Rev. C* **94**, 064310 (2016)
- [8] X. Q. Yang, L. J. Wang, J. Xiang, X. Y. Wu and Z. P. Li, *Phys. Rev. C* **103**, 054321 (2021).
- [9] G. -F. Berstch, M. Girod, S. Hilaire, J. -P. Delaroche, H. Goutte and S. Péru, *Phys. Rev. Lett.* **99**, 032502 (2007).
- [10] K. Nomura, T. Otsuka, R. Rodríguez-Guzmán, L. M. Robledo and P. Sarriguren, *Phys. Rev. C* **83**, 014309 (2011).
- [11] K. Nomura, T. Otsuka, R. Rodríguez-Guzmán, L. M. Robledo, P. Sarriguren, P. H. Reagan, P. D. Stevenson and Zs. Podolyak, *Phys. Rev. C* **83**, 054303 (2011).
- [12] K. Nomura, T. Otsuka, R. Rodríguez-Guzmán, L. M. Robledo and P. Sarriguren, *Phys. Rev. C* **84**, 054316 (2011).
- [13] K. Nomura, R. Rodríguez Guzmán and L. M. Robledo, *Phys. Rev. C* **94**, 044314 (2016); *Phys. Rev. C* **95**, 064310 (2017); *Phys. Rev. C* **96**, 014314 (2017); *Phys. Rev. C* **96**, 034310 (2017); *Phys. Rev. C* **96**, 064316 (2017); *Phys. Rev. C* **97**, 064313 (2018); *Phys. Rev. C* **97**, 064314 (2018); *Phys. Rev. C* **99**, 034308 (2019); *Phys. Rev. C* **101**, 014306 (2020).
- [14] J.-P. Delaroche, M. Girod, H. Goutte and J. Libert, *Nucl. Phys. A* **771**, 103 (2006).
- [15] H. Abusara, A.V. Afanasjev and P. Ring, *Phys. Rev. C* **82**, 044303 (2010).
- [16] R. Rodríguez-Guzmán and L. M. Robledo, *Phys. Rev. C* **89**, 054310 (2014).
- [17] S. E. Agbemava, A. V. Afanasjev, A. Taninah and A. Gyawali, *Phys. Rev. C* **99**, 034316 (2019).
- [18] P. A. Butler and W. Nazarewicz, *Rev. Mod. Phys.* **68**, 349 (1996).
- [19] R. Rodríguez-Guzmán and L. M. Robledo, *Eur. Phys. J. A* **53**, 245 (2017).
- [20] R. Rodríguez-Guzmán, Y. M. Humadi and L. M. Robledo, *Eur. Phys. J. A* **56**, 43 (2020).
- [21] M. Warda and L. M. Robledo, *Phys. Rev. C* **84**, 044608 (2011).
- [22] P. Möller, R. Bengtson, B. G. Carlsson, P. Olivius, T. Ichikawa, H. Sagawa and A. Iwamoto, *At. Data Nucl. Data Tables* **94**, 758 (2008).
- [23] W. Nazarewicz, P. Olanders, I. Ragnarsson, J. Dudek, G. Leander P. Möller, and E. Ruchowska, *Nucl. Phys. A* **429**, 269 (1984).
- [24] K. Nomura, D. Vretenar, T. Niksic and B.-N. Lu, *Phys. Rev. C* **89**, 024312 (2014).
- [25] K. Nomura, T. Niksic and D. Vretenar, *Phys. Rev. C* **97**, 024317 (2018).
- [26] K. Nomura, R. Rodríguez-Guzmán, and L. M. Robledo, *Phys. Rev. C* **92**, 014312 (2015).
- [27] K. Nomura, R. Rodríguez-Guzmán, Y. M. Humadi L. M. Robledo and J. E. García-Ramos, *Phys. Rev. C* **102**, 064326 (2020).
- [28] K. Nomura, R. Rodríguez-Guzmán, L. M. Robledo and J. E. García-Ramos, *Phys. Rev. C* **103**, 044311 (2021).
- [29] K. Nomura, R. Rodríguez-Guzmán, L. M. Robledo, J. E. García-Ramos and N. C. Hernández' *Phys. Rev. C* **104**, 044324 (2021).
- [30] K. Nomura, R. Rodríguez-Guzmán and L. M. Robledo, *Phys. Rev. C* **104**, 054320 (2021).
- [31] P. Bonche, S. J. Krieger, M. S. Weiss, J. Dobaczewski, H. Flocard, and P.-H. Heenen, *Phys. Rev. Lett.* **66**, 876 (1991).
- [32] Erler, K. Langanke, H. P. Loens, G. Martínez-Pinedo and P.-G. Reinhard, *Phys. Rev. C* **85**, 025802 (2012).
- [33] L. M. Robledo, M. Baldo, P. Schuck and X. Viñas, *Phys. Rev. C* **81**, 034315 (2010).
- [34] R. N. Bernard, L. M. Robledo, and T. R. Rodríguez, *Phys. Rev. C* **93**, 061302(R) (2016).
- [35] Z. P. Li, B. Y. Song, J. M. Yao, D. Vretenar and J. Meng, *Phys. Lett. B* **726**, 866 (2013).
- [36] L. M. Robledo and R. Rodríguez-Guzmán, *J. Phys. G: Nucl. Part. Phys.* **39**, 105103 (2012).
- [37] S. Y. Xia, H. Tao, Y. Lu, Z. P. Li, T. Niksic and D. Vretenar, *Phys. Rev. C* **96**, 054303 (2017).
- [38] S. E. Agbemava and A. V. Afanasjev, *Phys. Rev. C* **96**, 024301 (2017).
- [39] Y. Cao, S. E. Agbemava, A. V. Afanasjev, W. Nazarewicz and E. Olsen, *Phys. Rev. C* **102**, 024311 (2020).
- [40] L. M. Robledo and G. F. Bertsch, *Phys. Rev. C* **84**, 054302 (2011).
- [41] L. M. Robledo, *J. Phys. G: Nucl. Part. Phys.* **42**, 055109 (2015).
- [42] J. F. Berger, M. Girod, and D. Gogny, *Nucl. Phys. A* **428**, 23c (1984).
- [43] R. Rodríguez-Guzmán, L. M. Robledo and P. Sarriguren, *Phys. Rev. C* **86**, 034336 (2012).
- [44] L. M. Robledo and P. A. Butler, *Phys. Rev. C* **88**, 051302(R) (2013).
- [45] R. Rodríguez-Guzmán, Y. M. Humadi and L. M. Robledo, *J. Phys. G: Nucl. Part. Phys.* **48**, 015103 (2021).
- [46] R. Rodríguez-Guzmán and L. M. Robledo, *Phys. Rev. C* **103**, 044301 (2021).
- [47] R. Rodríguez-Guzmán and L. M. Robledo, *Phys. Rev. C* **108**, 024301 (2023).
- [48] S. Hilaire and M. Girod, *Eur. Phys. J. A* **33**, 237 (2005).
- [49] P. Möller, A. Sierk, T. Ichikawa, and H. Sagawa, *Atomic Data and Nuclear Data Tables* **109-110**, 1 (2016).
- [50] G. Scamps, S. Goriely, E. Olsen, M. Bender and W. Ryssens, *Eur. Phys. J. A* **57**, 333 (2021).
- [51] G. Lalazissis, S. Raman and P. Ring, *Atomic Data and Nuclear Data Tables* **71**, 1 (1999).
- [52] J. Engel and J. Menéndez, *Rep. Prog. Phys.* **80**, 046301 (2017).
- [53] L. Lotina and K. Nomura, *Phys. Rev. C* **109**, 034304 (2024).
- [54] R. Han, M. Warda, A. Zdeb and L. M. Robledo, *Phys. Rev. C* **104**, 064602 (2021).
- [55] P. E. Garrett, W. D. Kulp, J. L. Wood, D. Bandyopadhyay, S. Christen, S. Choudry, A. Dewald, A. Fitzler, C.

- Fransen, K. Jessen, J. Jolie, A. Kloezer, P. Kudejova, A. Kumar, S. R. Leshner, A. Linnemann, A. Lisetskiy, D. Martin, M. Masur, M. T. McEllistrem, O. Möller, M. Mynk, J. N. Orce, P. Pejovic, T. Pissulla, J. M. Regis, A. Schiller, D. Tonev and S. W. Yates, *J. Phys. G: Nucl. Part. Phys.* **31**, S1855 (2005).
- [56] A. A. Phillips, P. E. Garrett, N. Lo Iudice, A. V. Sushkov, L. Bettermann, N. Braun, D. G. Burke, G. A. Demand, T. Faestermann, P. Finlay, K. L. Green, R. Hertenberger, K. G. Leach, R. Krücken, M. A. Schumaker, C. E. Svensson, H.-F. Wirth and J. Wong, *Phys. Rev. C* **82**, 034321 (2010).
- [57] D. J. Hartley, F. G. Kondev, G. Savard, J. A. Clark, A. D. Ayangeakaa, S. Bottoni, M. P. Carpenter, P. Copp, K. Hicks, C. R. Hoffman, R. V. F. Janssens, T. Lauritsen, R. Orford, J. Sethi and S. Zhu, *Phys. Rev. C* **101**, 044301 (2020).
- [58] M. Spieker, S. Agbemava, D. Bazin, S. Biswas, P. Cottle, P. Farris, A. Gade, T. Ginter, S. Giraud, K. Kemper, J. Li, W. Nazarewicz, S. Noji, J. Pereira, L. Riley, M. Smith, D. Weisshaar, and R. Zegers, *Phys. Lett. B* **841**, 137932 (2023).
- [59] C. V. Nithish Kumar and L. M. Robledo, *Phys. Rev. C* **108**, 034312 (2023).
- [60] C. Gonzalez-Boquera, M. Centelles, X. Viñas and L. Robledo, *Phys. Lett. B* **779**, 195 (2018).
- [61] W. Ryssens, G. Giacalone, B. Schenke and C. Shen, *Phys. Rev. Lett.* **130**, 212302 (2023).
- [62] G. -F. Bertsch, *Phys. Lett. B* **26**, 130 (1968).
- [63] D. Hendrie, N. Glendenning, B. Harvey, O. Jarvis, H. Duhm, J. Saudinos and J. Mahoney, *Phys. Lett. B* **26**, 127 (1968).
- [64] L. M. Robledo, T. R. Rodríguez and R. R. Rodríguez-Guzmán, *J. Phys. G: Nucl. Part. Phys.* **46** 013001 (2019).
- [65] S. Goriely, S. Hilaire, M. Girod and S. Péru, *Phys. Rev. Lett.* **102**, 242501 (2009).
- [66] J. L. Egido and L. M. Robledo, *Nucl. Phys. A* **545**, 589 (1992).
- [67] L. M. Robledo and G. F. Berstch, *Phys. Rev. C* **84**, 014312 (2011).
- [68] L. M. Robledo, *Physical Review C* **50**, 2874 (1994); *Phys. Rev. C* **105**, L021307 (2022); *Phys. Rev. C* **105**, 044317 (2022).
- [69] R. R. Rodríguez-Guzmán, J. L. Egido and L.M. Robledo, *Nucl. Phys. A* **709**, 201 (2002).
- [70] P. Magierski, P.-H. Heenen and W. Nazarewicz, *Phys. Rev. C* **51**, R2880 (1995).
- [71] J. A. Sheikh, J. Dobaczewski, P. Ring, L. M. Robledo and C. Yannouleas *J. Phys. G: Nucl. Part. Phys.* **48** 123001 (2021).
- [72] L. M. Robledo, *Phys. Rev. C* **79**, 021302(R) (2009); *Phys. Rev. C* **84**, 014307 (2011)
- [73] G. -F. Bertsch and L. M. Robledo, *Phys. Rev. Lett.* **108**, 042505 (2022).